





Article

Synthesis and Evaluation of FeSX/TiO₂ for the Photocatalytic Degradation of Phenol under Visible-Light Region

Diego Alvarez-Bustos ¹, Felipe Sanchez-Minero ¹, Victor Santes ², Issis Claudette Romero-Ibarra ³, José Antonio de los Reyes Heredia ⁴, Reyna Rios-Escobedo ⁵, Francisco Tzompantzi-Morales ⁵ and Carlos Eduardo Santolalla-Vargas ^{2,*}

- ¹ Departamento de Ingeniería Química Petrolera, Instituto Politécnico Nacional, Zacatenco, Ciudad de Mexico C.P. 07738, Mexico; diegoalbu27@outlook.com (D.A.-B.); jfsmpipen@hotmail.com (F.S.-M.)
- ² Departamento de Biociencias e Ingeniería, Centro Interdisciplinario de Investigaciones y Estudios sobre el Medio Ambiente y Desarrollo (CIIEMAD), Instituto Politécnico Nacional, Ciudad de Mexico C.P. 07340, Mexico; vsantes@ipn.mx
- ³ Unidad Profesional Interdisciplinaria en Ingeniería y Tecnologías Avanzadas—Instituto Politécnico Nacional, Av. IPN No. 2580, Gustavo A. Madero, Ciudad de Mexico C.P. 07340, Mexico; iromero@ipn.mx
- ⁴ División de Ciencias Básicas e Ingeniería, Universidad Autónoma Metropolitana-Iztapalapa, Av. San Rafael Atlixco 186, Col. Vicentina, Ciudad de Mexico C.P. 09340, Mexico; jarh@xanum.uam.mx
- ⁵ Departamento de Ingeniería Química, Área de Catálisis, Universidad Autónoma Metropolitana-Iztapalapa, Av. San Rafael Atlixco 189, Col. Vicentina, Ciudad de Mexico C.P. 09340, Mexico; rios.escobedo.reyna@gmail.com (R.R.-E.); fjtz@xanum.uam.mx (F.T.-M.)
- * Correspondence: csantolallav@ipn.mx



Citation: Alvarez-Bustos, D.; Sanchez-Minero, F.; Santes, V.; Romero-Ibarra, I.C.; de los Reyes Heredia, J.A.; Rios-Escobedo, R.; Tzompantzi-Morales, F.; Santolalla-Vargas, C.E. Synthesis and Evaluation of FeSX/TiO₂ for the Photocatalytic Degradation of Phenol under Visible-Light Region. *Catalysts* **2022**, *12*, 457. <https://doi.org/10.3390/catal12050457>

Academic Editors: Hugo de Lasa and Salvador Escobedo

Received: 27 February 2022

Accepted: 11 April 2022

Published: 20 April 2022

Publisher's Note: MDPI stays neutral with regard to jurisdictional claims in published maps and institutional affiliations.

Abstract: In the present work, phenol was used as a model molecule to the photocatalytic evaluation of TiO₂ impregnated with iron sulphide and chlorine on a visible-light reactor. The iron–chlorine catalyst was prepared by incipient impregnation with the metal precursors, Fe(NO₃)₃ and NaCl on previously calcined TiO₂. The catalyst was sulphurized with H₂S at 300 °C for 1 h. The catalysts were prepared at different chlorine concentrations using HYDRA chemical equilibrium diagrams to obtain different fractions of FeCl⁺. The oxide catalysts were characterized with diffuse reflectance (DRS UV–Vis) and temperature programmed reduction analysis (TPR). Sulphurized catalysts were characterized with Raman spectrometry and X-ray photoelectron spectrometry (XPS). The FeS–2Cl/TiO₂ catalyst presented 8.35 times higher photodegradation than TiO₂ and 6.4 times higher compared to the FeS–0.25Cl/TiO₂ catalyst. DRS and XPS showed similar results of band gap, proving that the catalyst remain stable after sulphurisation. The TPR results of FeS–2Cl/TiO₂ showed an increment of 86.29% in Fe²⁺/Fe³⁺ compared to FeS–0.25Cl/TiO₂. XPS and Raman results for oxide and sulphated iron species relation suggested that FeS–2Cl/TiO₂ decreased 4.45% compared to FeS–0.25Cl/TiO₂ catalyst. XPS semiquantitative for S/Fe results showed that the FeS–2Cl/TiO₂ catalyst increased 73.17% in comparison to FeS–0.25Cl/TiO₂. These results suggested the increment of sulphurisation degree for FeS–2Cl/TiO₂. In this regard, the catalyst characterization results showed that the presence of FeCl⁺ (0.85 fractions) in solution before impregnation promoted the active sulphide species maintaining the band gap and improved the degradation of phenol on visible light.

Keywords: degradation; photocatalysis; phenol; impregnation



Copyright: © 2022 by the authors. Licensee MDPI, Basel, Switzerland. This article is an open access article distributed under the terms and conditions of the Creative Commons Attribution (CC BY) license (<https://creativecommons.org/licenses/by/4.0/>).

1. Introduction

In industrial wastewater, the main parameters treatment are high loads of dissolved organic compounds. These pollutants are difficult to remove with the processes commonly used to treat domestic wastewater [1,2]. The Political Constitution of the United States of Mexico confers inalienable rights of ownership over all national waters to the nation [3], providing the foundation for water protection and management laws for hydraulic resources to be exploited [3]. The current legal framework governing water pollution control is set forth in two laws: the General Law of Ecological Balance and Environmental Protection,

which establishes general criteria pertaining to water pollution prevention and control; and the National Waters Law, which provides a comprehensive legal regime that supports the broader provisions set out in the Ecology Law [3].

Phenolic compounds exist in water bodies due to the discharge of polluted wastewater from industrial, agricultural, and domestic activities into water bodies [4]. These compounds are known for being toxic and inflict severe and long-lasting effects on humans and animals, acting as carcinogens and causing damage to the red blood cells and the liver even in low concentrations [4]. The interaction of phenolic compounds with organic material in water can produce substituted compounds or other moieties, which may be as toxic as the original phenolic compounds [4]. Specific emphasis is placed on the techniques of their removal from water with attention paid to conventional and advanced methods. Among these methods are ozonation, adsorption, extraction, photocatalytic degradation, biological, electro-Fenton, adsorption and ion exchange and membrane-based separation [4]. In this regard, emerging technologies are based on efficiently degrading the dissolved solids present in wastewater, some of the most used technologies are advanced oxidation processes (AOP).

AOP is a highly effective novel method speeding up the oxidation process. AOP can combine with ozone (O_3), catalyst, or ultraviolet (UV) irradiation to offer a powerful treatment of wastewater [5]. Several AOP's such as O_3 , O_3/H_2O_2 , UV, UV/ O_3 , UV/ H_2O_2 , $O_3/UV/H_2O_2$, Fe^{2+}/H_2O_2 and photocatalysis processes had been investigated for the oxidation of phenol in an aqueous medium [6]. Among all, the Fenton process showed the fastest removal rate for phenol in wastewater; the lower costs were observed for ozonation, and single ozonation provides the best results for phenol degradation in ozone combinations [5].

One of the techniques that has gained a lot of attention due to its potential for scale-up is heterogeneous photocatalysis [7]; this technique consists of a semiconductor material, which is irradiated with photons of appropriate energy, undergoing excitation of the electrons located in its valence band to its conduction band [8]. This allows for the formation of a redox couple that interacts with the adsorbed species and can lead to the oxidation of pollutants (phenol) [8]. The main sub-products related to photocatalytic phenol degradation include hydroquinone, used in the treatment of ephelides (freckles), melasma, post-inflammatory hyperpigmentation and actinic lentigo; benzoquinone, used as a fungicide, a photographic reagent and in the manufacture of dyes and other chemicals; catechol, used as an astringent and as an antiseptic in photography and in the electroplating and processing of other chemicals; and oxalic acid, used as a deoxidising agent to clean radiators and to remove ink stains. These high-value-added sub-products make photocatalytic degradation a profitable technique for phenol treatment. The photocatalytic properties of metal oxide catalysts are due to the fact that excitation of electrons from the valence to the conduction band of the catalyst occurs upon its irradiation with light of the appropriate wavelength [4]. The promotion of the electrons (e^-) creates positive charges or holes (h^+) on the valence band, and an accumulation of electrons on the conduction band of the catalyst the generation of these charge carriers (e^- and h^+) initiates the photocatalytic degradation process [9]. The valence band holes attack and the oxidized surface absorbs water molecules to form hydroxyl radicals (OH^*) [10]. Conduction band electrons reduce oxygen molecules and produce oxygen radicals or superoxide radicals (O_2^*) [10]. Highly reactive radicals attack and convert the pollutants to harmless products such as carbon dioxide and water [10,11]. The photocatalytic degradation of phenolic compounds from wastewater has been demonstrated by many researchers using various catalysts including TiO_2 /reduced graphene [12,13], ZnO [14], Fe_2O_3 decorated on carbon nanotubes [15] and CuO [16].

Several reports have shown that photocatalytic degradation techniques have been utilized effectively to degrade phenol from the water [13]. The results confirmed that using zeolite as support for FeO enhancement promotes efficient photocatalytic degradation [17]. The improved photocatalytic activity of the FeO–zeolite composite was attributed to the fact

that the zeolite prevented agglomeration of the FeO nanoparticles and minimized the charge carrier recombination rate [17]. F. Shahrezaei, A. Akhbari, and A. Rostami. [18] explored the photocatalytic degradation ability of TiO₂ in the degradation of phenolic compounds present in wastewater from a refinery [18]. The highest degradation efficiency of the phenol and its derivatives was identified at an optimum temperature of 318 K, pH 3 and 100 mg/L catalyst concentration [18]. A 90% degradation efficiency of phenol was achieved within 2 h at these optimum conditions. Guangping Zeng, Qiaoling Zhang, Youzhi Liu, Shaochuang Zhang, and Jing Guo [19] explored the photocatalytic degradation of Toluene with FeO–TiO₂, showing an improvement of 58% in the degradation rates compared to TiO₂ P25 [19]. Increasing the concentration from 0.5% to 5.0% of Fe³⁺ results in a reduction in the band gap energy from 3.06 eV in undoped Fe to 2.86 eV and 2.26 eV. Fe³⁺ not only broadens the photo response range but also effectively suppresses the recombination of the electron and hole [19]. As a result, the catalytic activity was enhanced. The degradation rate of 1.0% Fe–TiO₂ to toluene of 105 ppm reached 95.7% after 4 h under UV light [19]. The chlorine doping effect was explored by Zhen Cao, Tingting Zhang, Pin Ren, Ding Cao, Yanjun Lin, Liren Wang, Bing Zhang, and Xu Xiang [20]. The investigation reported that chloride ions adsorbed onto the TiO₂ surface, introducing a negative surface charge that enhances the electrostatic adsorption of cationic dyes, and greatly improves the self-sensitizing degradation performance of the dyes [20]. Chloride ions replace lattice oxygen atoms in TiO₂, inducing lattice oxygen vacancies that reduce the apparent bandgap of the TiO₂ particles, enhancing its absorption of visible light and further increasing the photocatalytic activity of the composite-coated fabric [20]. Y. Niu, M. Xing, J. Zhang, and B. Tian [21] reported the beneficial co-effects between S doping and Fe(III) on phenol photodegradation; doping decreased the bandgap energy due to the formation of impurity levels and suppressed the recombination of electrons and holes by trapping electrons, leading to higher the photoactivity of Fe single-bond S-co doped TiO₂ compared to that of undoped and S-doped TiO₂.

Within this scenario, the purpose of the present investigation was to study the influence of chlorine and sulphur on an FeO–TiO₂ catalyst prepared by incipient impregnation. In this regard, the chlorine will modify the iron sphere coordination in order to form FeCl species complexes in the impregnation solution. The FeCl species complexes could improve the formation of the FeS phase in the FeO–TiO₂ catalysts after sulfurization activation. The aqueous impregnation solutions of the FeCl species complexes, dried solids and sulphated catalysts were characterized by different physicochemical techniques such as DRS UV–Vis, TPR, Raman and XPS. The oxide and sulphated catalyst activity were evaluated by UV–Vis and TOC techniques on a visible-light reactor.

2. Results

2.1. Solution Analysis

HYDRA Formulation

The impregnation solutions were carried out with the HYDRA-Medusa [22] chemical equilibrium diagrams program to obtain different fractions of FeCl⁺. Several diagrams were constructed considering the concentration variation derived from metal precursor salts and pH adjusters. The ionic strength effect was considered due to the high ionic concentration in experimental solutions [23,24]. All calculations were carried out at a standard temperature (298 K) and fixed molar concentrations of Fe and Cl. In this regard, five mixed solutions were formulated with iron solution concentration at 5.68 M and different ratios iron/chlorine (ratio: 0.25, 0.5, 1, 2 and 3). The photocatalysts will be referred to by the acronyms: Fe–0.25Cl, Fe–0.5Cl, Fe–Cl, Fe–2Cl and Fe–3Cl. Figure 1 shows the presence of the FeCl⁺ species with the lowest ratio, 0.25; ratio 2.0 showed the highest fraction of the FeCl⁺ species, as shown in Figure 2.

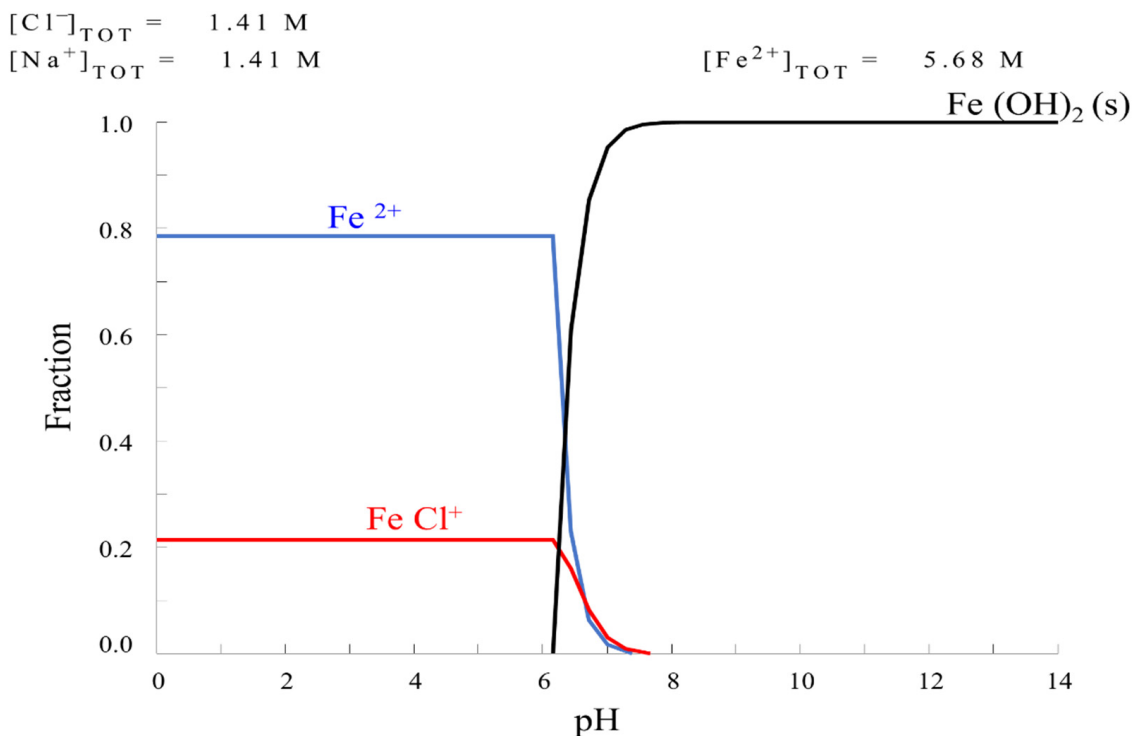


Figure 1. Chemical equilibrium diagram for solution iron/chlorine ratio at 0.25.

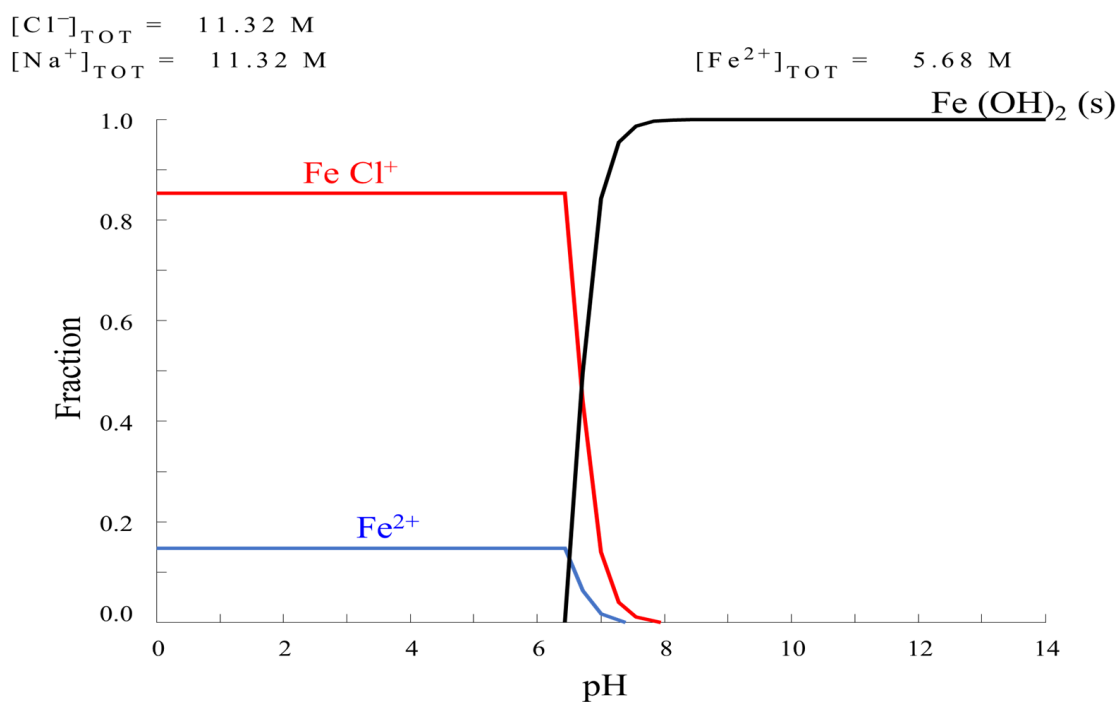


Figure 2. Chemical equilibrium diagram for solution iron/chlorine ratio at 2.0.

2.2. Catalyst Characterization

2.2.1. Oxide Catalyst

DRS UV–VIS Spectroscopy

DRS UV–Vis spectroscopy analyses were performed to study the optical absorption properties. The UV–Vis spectra for FeCl/TiO₂ catalysts are shown in Figure 3. The TiO₂ spectrum exhibited a band in the range of 200–390 nm corresponding to O²⁻ → Ti⁴⁺ charge

transfer [25]. For the Fe catalysts, three regions can be distinguished in the ranges 200–300, 300–400 and 400–650 nm. The band at approximately 200–300 nm is associated with charge transfer $O \rightarrow Fe^{3+}$, which indicates that Fe^{3+} could be incorporated as isolated cations [26]. The band between 300 and 400 nm corresponds to isolated Fe^{3+} ions in tetrahedral coordination [26]. Additionally, the band about 400–650 nm indicated the presence of Fe_2O_3 or Fe_3O_4 in octahedral coordination [27]. The absorption edges for the $FeCl_3$ - TiO_2 and Fe_2O_3 - TiO_2 catalysts compounds shifted to the visible region as a result of electronic interactions. A displacement over bands was presented as the chlorine concentration increased. The band at approximately 750–900 nm confirmed that the Fe_2O_3 nanoparticles present on the catalysts exhibit absorption in the visible-light range. These results could suggest the feasibility of utilization of visible light for photo-catalysis [28]. Additionally, this result could be indicated the modification of Fe sphere coordination and effective surface hybridization between the species between $FeCl_3$, Fe_2O_3 , and TiO_2 [25]. Additionally, the TiO_2 spectra showed that the structure of the TiO_2 support is not affected by iron–chlorine impregnation [29].

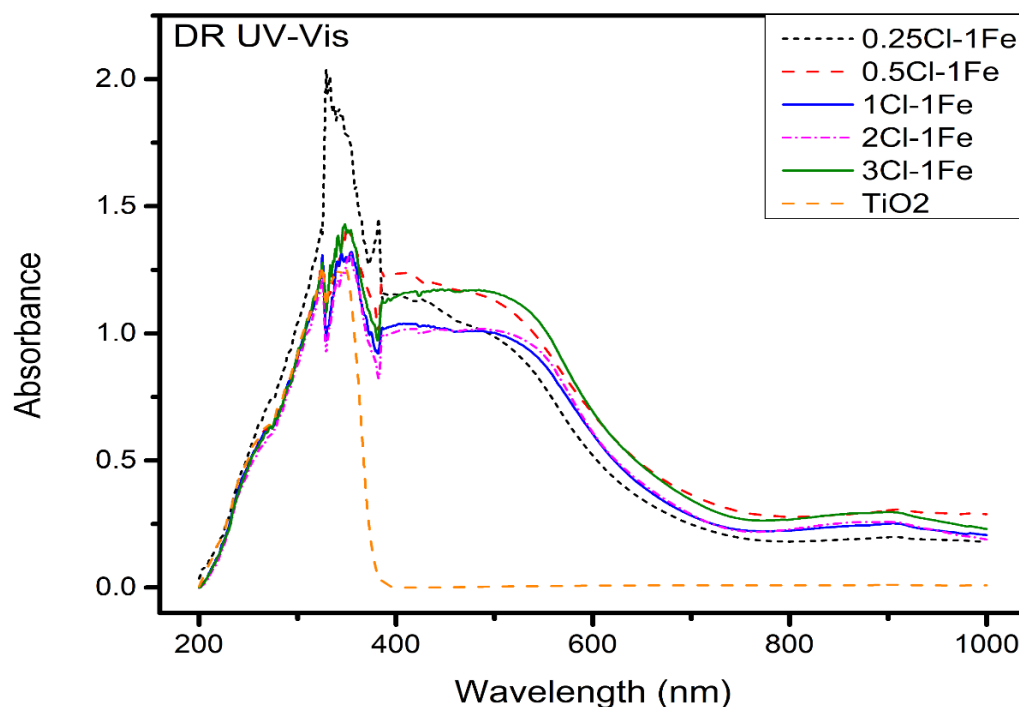


Figure 3. DRS UV-Vis for Fe–0.25Cl, Fe–0.5Cl, Fe–1.0Cl, Fe–2.0Cl and Fe–3.0Cl oxide catalyst.

After recalculating the spectra with the Kubelka–Munk function, the tangent to the Tauc curve was used to determine the bandgap energy [25]. The bandgap energy of the catalyst Fe–2Cl is presented in Figure 4. The bandgap energy calculations of the catalysts by the Kubelka–Munk formula is as follows:

$$A = -\lg(R)$$

$$F(R) = (1 - R)^2/2R$$

$$E = 1240/\lambda$$

where A is the absorbance, R is the reflectivity, E is the bandgap energy, and λ is the optical wavelength. The bandgap energy diagram of the sample was obtained by using $(F(R) * E)^{1/2}$ as the longitudinal coordinate and E as the transverse coordinate [25]. As in the method described by Tauc, the linear fit of the fundamental peak was applied. Additionally, a linear fit used as an abscissa is applied for the slope below the fundamental absorption [30]. The results of the bandgaps are presented in Table 1. The TiO_2 presented 3.3 eV while the

catalysts with iron and chlorine presented 2.9 a 3.01 eV. In contrast, the incorporation of iron species improves metal character. The results showed that the addition of chlorine reduces the band gap energy more compared to TiO₂. However, the incremental chlorine concentration does not continue reducing the bandgap compared to other chlorine-doped catalysts. The bandgap variation could be related with the formation of Fe²⁺ species on the catalyst. Fe²⁺ species are directly related to chlorine addition.

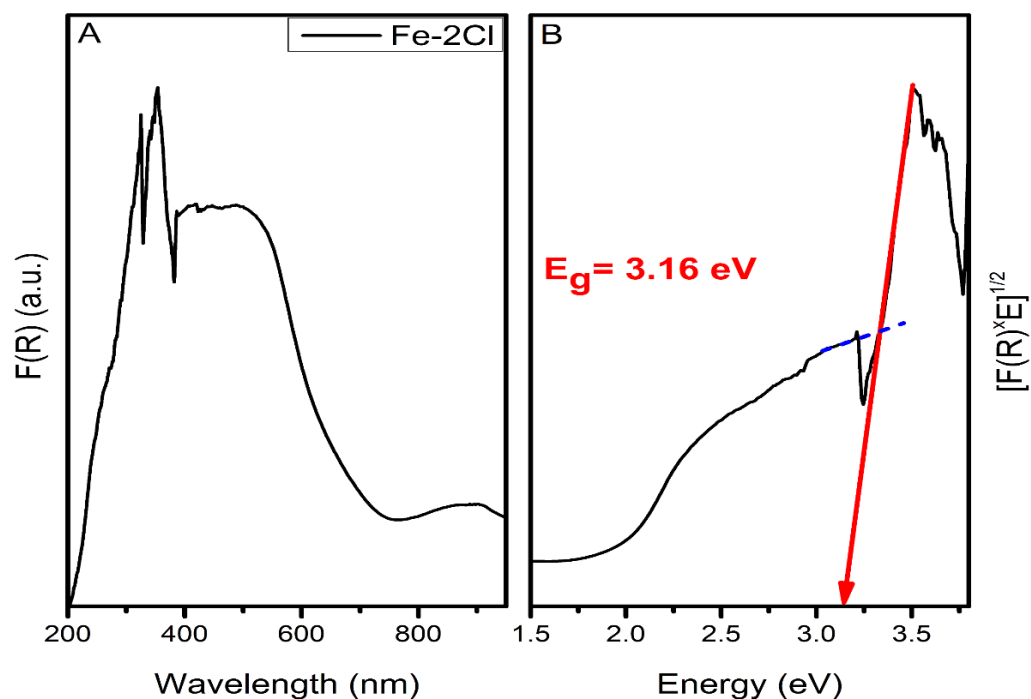


Figure 4. (A) Diffuse reflectance spectroscopy, F(R) versus wavelength, and (B) Tauc Plot $E_g = 3.10$ eV for Fe-2Cl catalyst.

Table 1. Band Gap of catalyst.

Catalyst	Band Gap
TiO ₂	3.3
Fe-0.25Cl	3.06
Fe-0.5Cl	3.0
Fe-Cl	3.12
Fe-2Cl	3.16
Fe-3Cl	3.08

Temperature-Programmed Reduction Analysis

TPR profiles are presented in Figure 5. TPR characterization was used to observe the reduction temperatures states of the photocatalysts. TPR profiles for the catalysts presented a principal peak between 400 and 600 °C related to Fe³⁺ to Fe²⁺. Additionally, the catalysts exhibited a displacement corresponding to the increase in chlorine species concentration on the reduction temperature of Fe³⁺ to Fe²⁺. In addition, the increase in chlorine concentration showed a lower reduction temperature of Fe²⁺ to Fe⁰ above 600 °C. The deconvolution peaks for one catalyst are shown in Figure 6. The Fe-2Cl material exhibited a maximum peak at 600 °C and a shoulder at 440 °C corresponding to the reduction in Fe³⁺ species. Additionally, the Fe-2Cl catalyst presented a shoulder with a maximum peak at 674 °C corresponding to the reduction of Fe³⁺ to Fe²⁺ and Fe⁰ species [31]. The last peak with

a maximum observed at 901 °C is attributed to Fe species with a strong metal–support interaction [32]. The areas of the observed peaks were performed through deconvolutions.

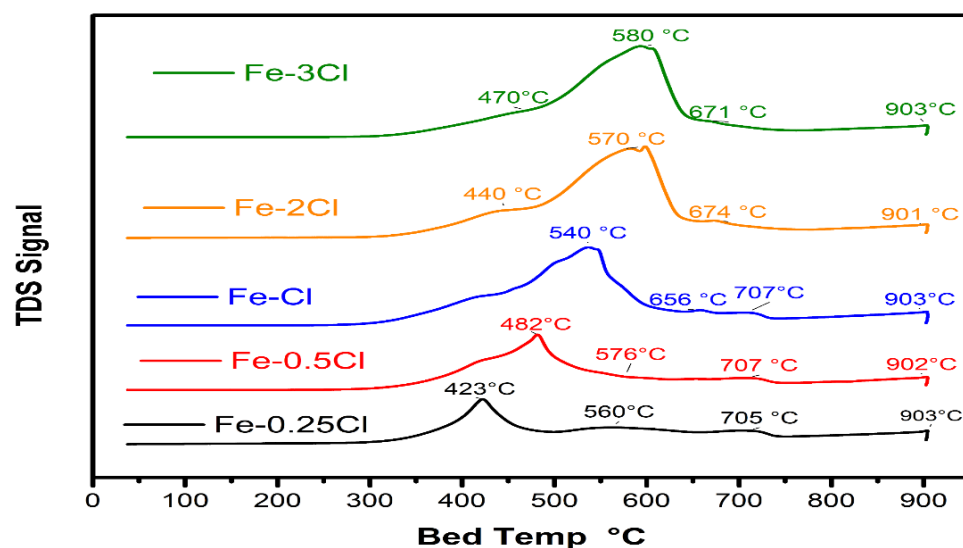


Figure 5. Temperature-programmed profiles for Fe-0.25Cl, Fe-0.5Cl, Fe-1.0Cl, Fe-2.0Cl and Fe-3.0Cl oxide catalyst.

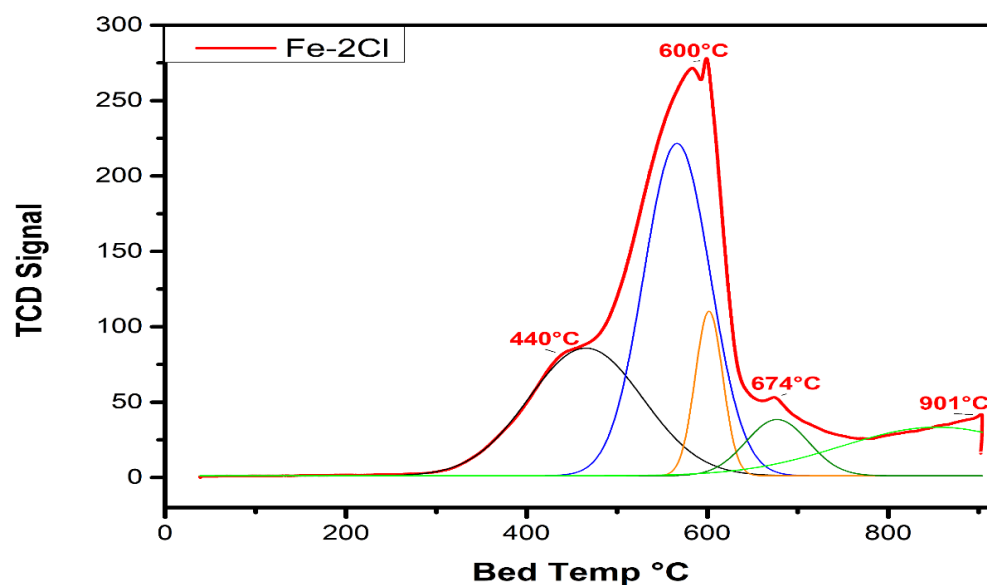


Figure 6. Temperature-programmed deconvolution for Fe-2Cl oxide catalyst.

The deconvolution results of the TPR analysis of the oxide catalysts are presented in Table 2. Table 2 shows the reduction temperatures for the photocatalysts and the Fe species areas. The first iron reduction temperature between 400 and 550 °C presented shifted as the chlorine concentration increased. In addition, the second iron reduction temperature between 550 and 650 °C showed a shift in equilibrium for the catalyst Fe-2Cl and Fe-3Cl. Additionally, these results suggested an increase in Fe²⁺ species for Fe-2Cl at a lower reduction temperature and, consecutively, there was a weaker metal–support interaction in comparison with the Fe-Cl (ratio: 0.5, 1.0, 3.0).

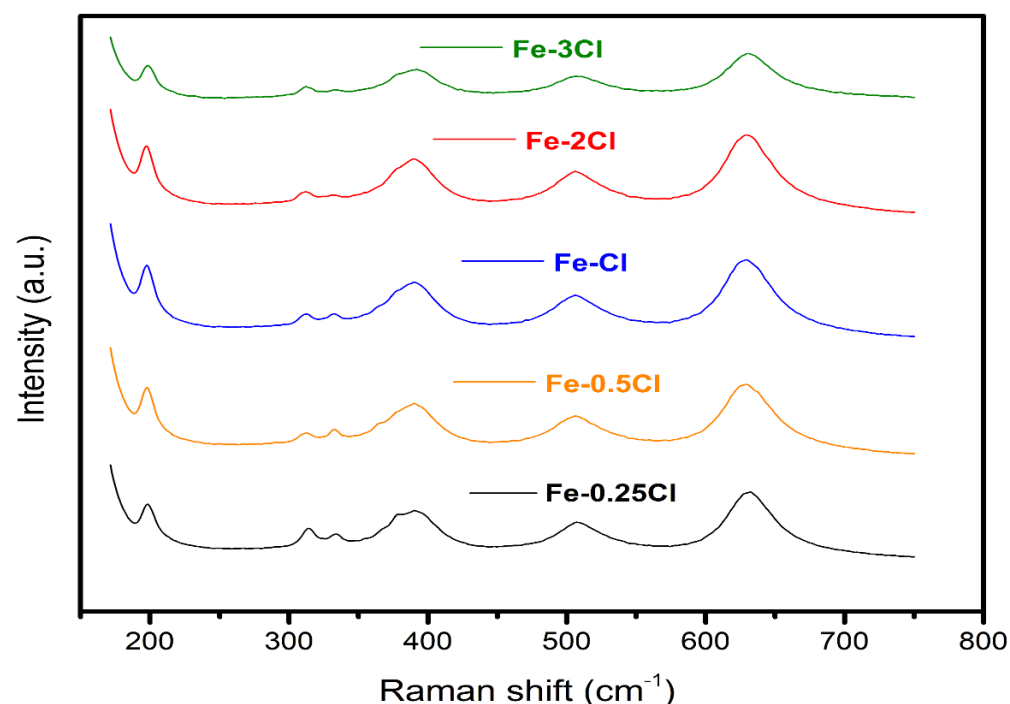
Table 2. Catalyst reduction temperatures and areas.

Catalyst	Redox Temperature	Area	Redox Temperature	Area	Redox Temperature	Area
Fe-0.25Cl	423 °C	7099.04	560 °C	754.21	903 °C	9336.55
Fe-0.5Cl	482 °C	17,797.61	576 °C	1865.48	902 °C	5043.24
Fe-Cl	540 °C	16,684.97	656 °C	9459.16	903 °C	4023.66
Fe-2Cl	440 °C	4173.65	570 °C	3233.58	901 °C	8592.72
Fe-3Cl	470 °C	16,352.44	580 °C	13,804.88	903 °C	1255.82

2.2.2. Sulphated Catalyst

Raman Spectroscopy

The sulphated catalysts were measured by Raman spectroscopy. All Raman samples are presented in Figure 7. The Raman spectra for Fe-Cl (ratio: 0.25, 0.5, 1.0, 2.0 and 3.0) showed bands corresponding to TiO₂ anatase compounds centred at 150, 400, and 500 cm⁻¹ [33]. Three Raman vibration modes were observed at 313, 332 and 390 cm⁻¹ corresponding to FeS species [34]. On the other hand, the ratio intensity with the vibrations at 198, 506, and 630 cm⁻¹ is related to the iron oxide species [35]. In this sense, Raman spectroscopy was used to determine sulphated and oxide compounds. Sulphated and oxide species were represented with the acronym Fe-Sy and Fe-Ox, respectively. Additionally, a close-up of the Raman spectrum from 190 to 800 cm⁻¹ is shown, where the characteristic bands of the Fe₂O₃, FeCl₃, FeS species in the five sulphated catalysts are qualitatively presented.

**Figure 7.** Raman spectra for FeS-0.25Cl, FeS-0.5Cl, FeS-1.0Cl, FeS-2.0Cl and FeS-3.0Cl catalysts.

The catalyst deconvolution example of Raman spectra is presented in Figure 8. The deconvolution was performed to obtain the Fe-Ox, Fe-S, and Fe-Cl species. In addition, a relation between the Fe-Sy and Fe-Ox ratios ((Fe-Sy)/(Fe-Ox)) is shown in Table 3. The catalysts FeS-0.25Cl, FeS-0.5Cl, FeS-1.0Cl, FeS-2.0Cl and FeS-3.0Cl presented 0.62, 0.61, 0.61, 0.60 and 0.60 sulfidation degree, respectively. These results suggested the formation of FeS species.

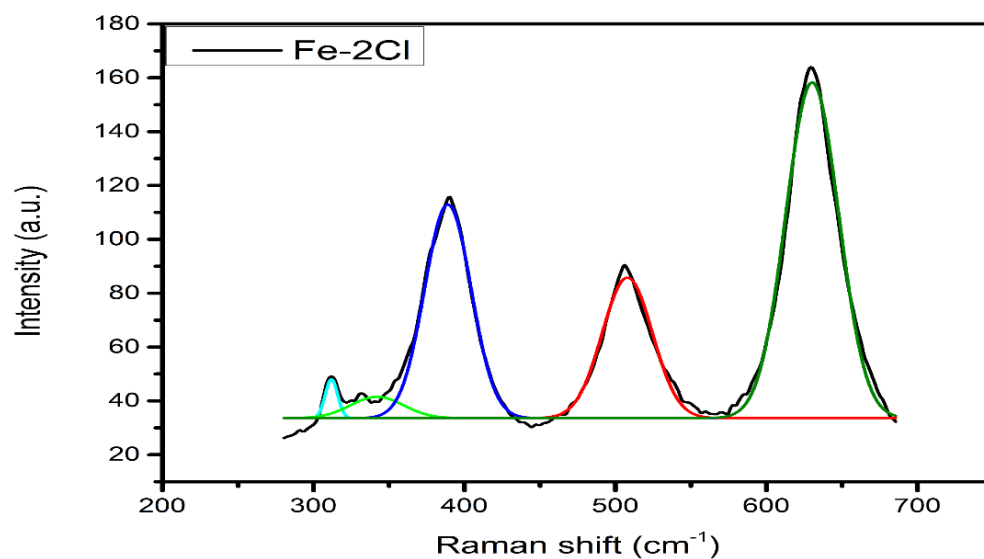


Figure 8. Deconvolutions of Raman spectra of the sulphur catalyst (FeS-2Cl).

Table 3. Sulfide-Oxide ratio from Raman spectra.

Catalyst	Fe-Sy	Fe-Ox	$\frac{\text{Fe-Sy}}{\text{Fe-Ox}}$
FeS-0.25Cl	2900.29	1745.30	0.6243
FeS-0.5Cl	3175.45	1992.05	0.6145
FeS-Cl	3486.89	2218.10	0.6112
FeS-2Cl	3390.54	2172.28	0.6095
FeS-3Cl	2038.7	1366.44	0.6050

X-ray Photoelectron Spectroscopy (XPS)

The chemical states of the iron-sulphide species were examined by XPS analysis. The XPS spectrum for FeS-2Cl catalyst is presented in Figures 9 and 10.

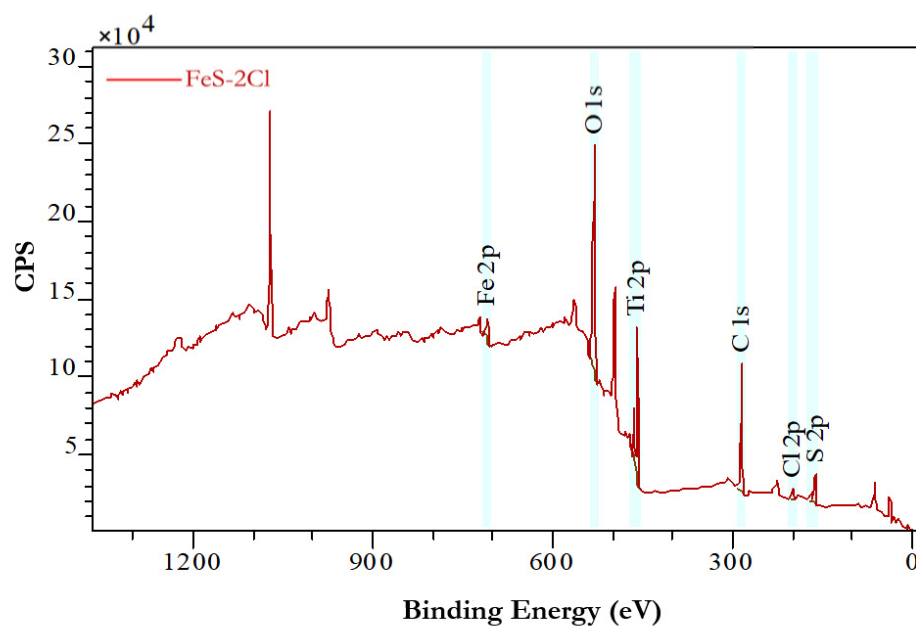


Figure 9. XPS spectrum for FeS-2Cl catalyst.

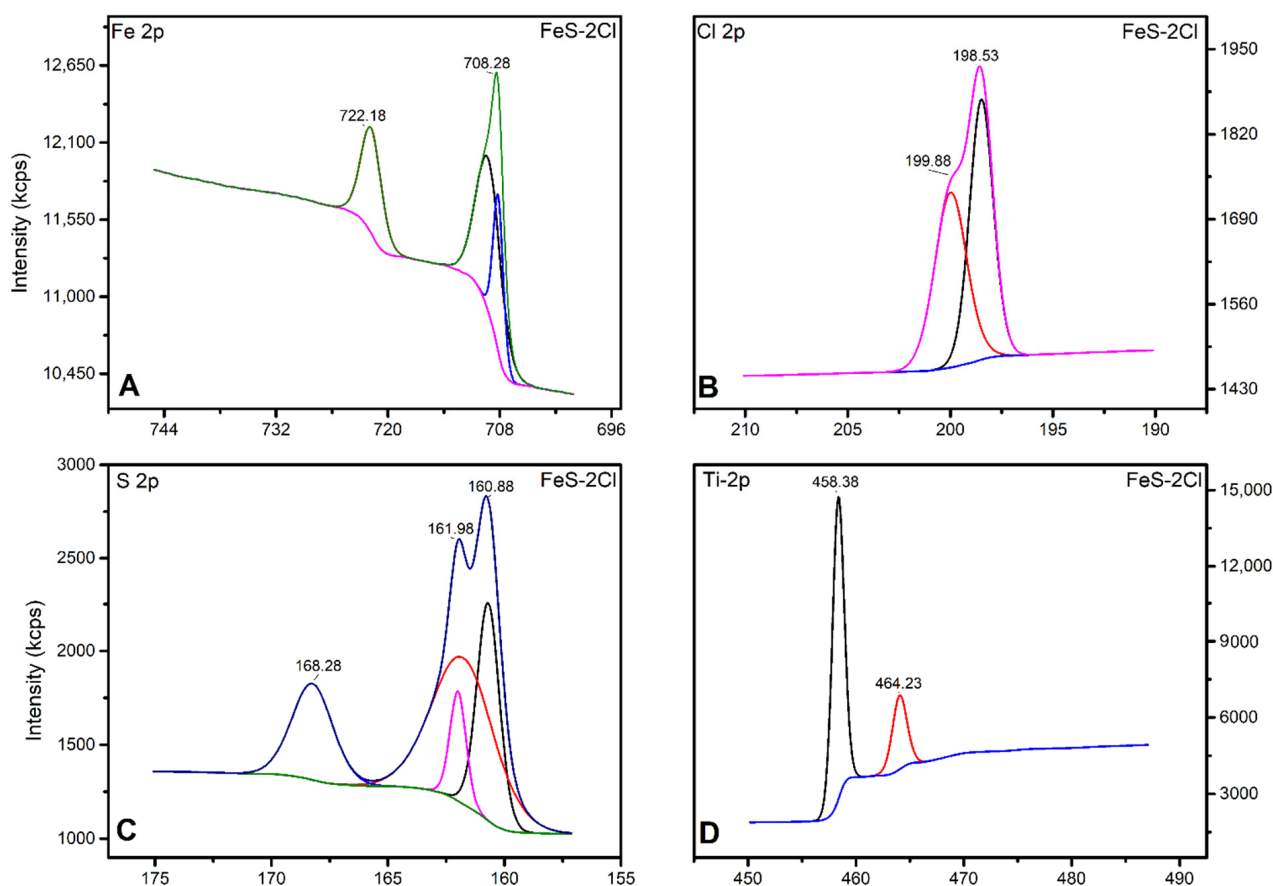


Figure 10. XPS spectrum for catalyst FeS-2Cl. (A) Fe 2p, (B) Cl 2p, (C) S 2p and (D) Ti 2p.

Figure 9 shows the binding spectra of Fe 2p centred at 708.08 eV, Cl 2p centred at 199.08 eV and S 2p centred at 161.08 eV for FeS-2Cl catalyst, respectively.

Figure 10 shows the high-resolution spectra for Fe, Cl, S, and Ti. The Fe 2p_{1/2} and Fe 2p_{3/2} peaks were centred, respectively, at 708.28 eV and 722.18 eV and the separation ($\Delta = 2p_{1/2} - 2p_{3/2}$) was 13.9 eV, which are attributed to Fe²⁺ states from the FeS phase [36] (Figure 10A).

The FeS-0.25Cl, FeS-0.5Cl and FeS-Cl catalysts show the characteristic peaks of Fe³⁺ iron oxides (710.5 eV, 723.4 eV) [36], with displacement due to Fe-Cl interactions [37]. However, the FeS-3Cl catalyst shows the characteristic Fe³⁺ oxide bands and a peak with a smaller Fe²⁺ distinctive band area corresponding to FeS.

The FeS-2Cl catalyst presented peaks at 722.1 eV and 708.2 eV, corresponding to Fe²⁺ of FeS [36,37]. The two peaks at 198.53 eV and 199.88 eV are observed in the Cl 2p, as shown in Figure 10B. These peaks are due to the 2p_{3/2} and 2p_{1/2} electrons of the ionic chlorine (Cl⁻) [37]. Additionally, Cl 2p presented the binding energy of chlorine at 198.53 eV, which was attributed to FeCl₃ [38].

Photocatalysts showed the characteristic peaks of the Cl- species corresponding to the Fe-Cl bond. In addition, photocatalysts FeS-0.5Cl, FeS-Cl, and FeS-2Cl exhibited an additional peak of a smaller area corresponding to the C-Cl bonds [37].

Two peaks at 168.28 eV and 161.98 eV can be attributed to S 2p_{3/2} and S 2p_{1/2}, respectively. These peaks are related to FeS (Figure 10C) [36].

The Fe with chlorine at different ratios showed characteristic peaks of the S 2p species corresponding to the FeS bond. Additionally, the spectra showed a shift due to the effect of Cl on the catalysts [37].

The binding energy of Ti 2p_{1/2} and Ti 2p_{3/2} was observed to be approximately 464.23 eV and 458.38 eV, respectively. In addition, the splitting data between the Ti 2p_{1/2} and Ti 2p_{3/2} core levels are 5.85 eV, indicating a normal Ti⁴⁺ state in the TiO₂

anatase [39]. These results showed that the TiO_2 anatase phase had been successfully introduced into FeS nanostructures (Figure 10D) [36].

The Band Gap calculus was realized with the O 1s spectra region (Figure 11). The O 1s spectra shows the presence of two types of oxygen on the surface of the intercalation compounds. The peak at the binding energy of 529 eV and 530 eV may be due to oxygen bound to Fe (Fe–O) [38]. Oxygen in the form of water in the intercalation compounds is shown at the peak binding energy of 531 eV [37].

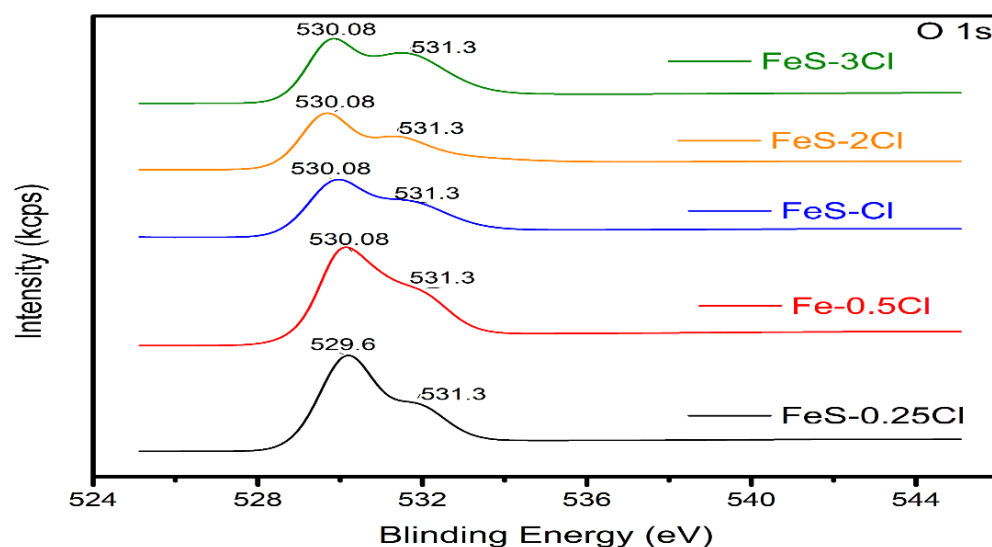


Figure 11. XPS O 1s diagram of all sulphur catalysts.

The energy loss spectra of O 1s were used to determine the bandgap. The bandgap denotes the energy separation between the peak energy and the threshold of inelastic losses corresponding to electronic band-to-band transitions and excitation of plasma waves below the Fermi level with electrons in the VB [40]. The start of the energy loss spectrum is obtained by linear extrapolation from the maximum negative slope segment to the background level [41]. The method of the energy loss peak was used for the corresponding O 1s spectrum. The E_g value of a large bandgap can be determined. Therefore, the procedure to obtain E_g includes a linear curve fit of the measured loss spectrum near the onset of inelastic losses [40]. The determination of the E_g for the materials with a large bandgap using the peak energy loss of the O 1s spectrum has been widely reported. In this context, XPS is useful to analyse the inelastic collisions that occur during photoexcitation and electron photoemission of materials.

Figure 12 shows the plots of the high-resolution scan of the O 1s core level for the catalysts FeS–0.5Cl, FeS–Cl, and FeS–2Cl.

Table 4 presents the photocatalysts conduction band results that were calculated from XPS diagrams [42–44]. The results will be discussed in Section 3.

Table 4. Band gap, valence band and conduction band sulphide catalyst.

XPS	Band Gap	Valence Band	Conduction Band
FeS–0.25Cl	2.90	2.27	–0.63
FeS–0.5Cl	2.82	3.13	–0.31
FeS–Cl	3.10	2.99	–0.11
FeS–2Cl	3.05	1.97	–1.08
FeS–3Cl	2.95	3.05	0.10

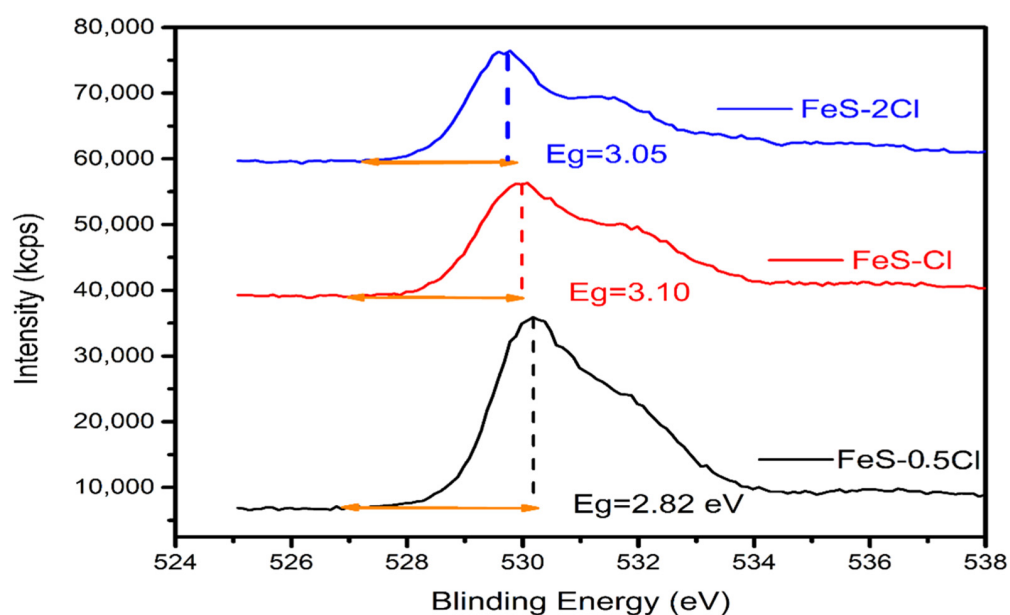


Figure 12. XPS O 1s band gap diagram, sulphur catalysts.

Table 5 the FeS–0.25Cl, FeS–0.5Cl, FeS–1.0Cl, FeS–2.0Cl and FeS–3.0Cl presented 0.64, 0.64, 0.63, 0.61 and 0.60 sulfidation–oxide ratio. These results suggested a higher concentration of FeSy species in comparison with FeOx for the photocatalysts. This result is in agreement with Raman results.

Table 5. Oxide and sulphide areas from Fe 2p XPS spectra.

XPS	Fe ³⁺ (Oxide)	Fe ²⁺ (Sulphide)	Relation $\frac{S_y}{O_x}$
FeS–0.25Cl	6911.51	11,746.8	0.6464
FeS–0.5Cl	13,946.1	42,509.4	0.6404
FeS–Cl	6307.06	8236.48	0.6351
FeS–2Cl	3246.41	5244.27	0.6176
FeS–3Cl	5483.04	8358.71	0.6038

2.3. Photocatalytic Activity

Figure 13 shows the photocatalytic activity for oxide and sulphide catalysts on the visible-light region. Additionally, Table 6 presents the results of degradations for dark, photolysis, oxide and sulphide catalysts. Reaction in dark condition presented an absorption of 3.8%. Reaction without catalyst (photolysis) and TiO₂ presented degradation of 5.77, and 7.77%, respectively. The Fe–0.25Cl, Fe–2Cl and Fe–3Cl oxide catalysts presented 12.5, 28.9 and 26.7% of phenol degradation, respectively. The Fe–0.25Cl, Fe–2Cl and Fe–3Cl sulphide catalysts presented 29.2%, 48.5% and 42.4% of phenol degradation, respectively. The degradation for sulphated catalysts increased until 50% after 6 h. These results suggest an increase of 40% c.a. on catalytic activity for sulphated catalysts than oxide catalysts.

The photocatalytic activity presented non-linear degradation. This degradation could be related to the formation of intermediate products, a variation in air flux, and catalyst distribution over the reactor.

Total Organic Carbon (TOC) Analysis

The TOC results for sulphated catalysts are presented in Figure 14. The mineralization percentage for FeS–0.25Cl, FeS–0.5Cl, FeS–2Cl and FeS–3Cl catalysts presented 11.0%, 10.0%, 40.0% and 23.0%, respectively. The highest mineralization was exhibited for FeS–2Cl while

the lowest mineralization values were showed for FeS–0.25Cl, and FeS–0.5Cl sulphated catalysts. These results are in agreement with photocatalytic activity results.

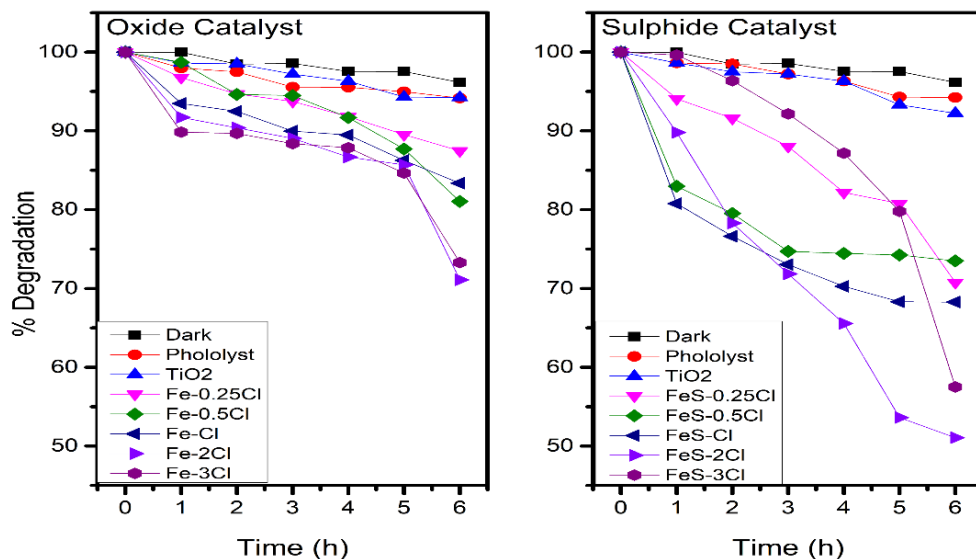


Figure 13. Phenol degradation with oxide and sulphide catalyst.

Table 6. Degradation results on visible-light region.

Oxide	% Degradation	Sulphide	% Degradation
Dark	3.8	Dark	3.8
Photolysis	5.77	Photolysis	5.77
TiO ₂	5.85	TiO ₂	7.87
Fe–0.25Cl	12.5	FeS–0.25Cl	29.2
Fe–0.5Cl	18.9	FeS–0.5Cl	26.4
Fe–Cl	16.6	FeS–Cl	31.7
Fe–2Cl	28.9	FeS–2Cl	48.5
Fe–3Cl	26.7	FeS–3Cl	42.4

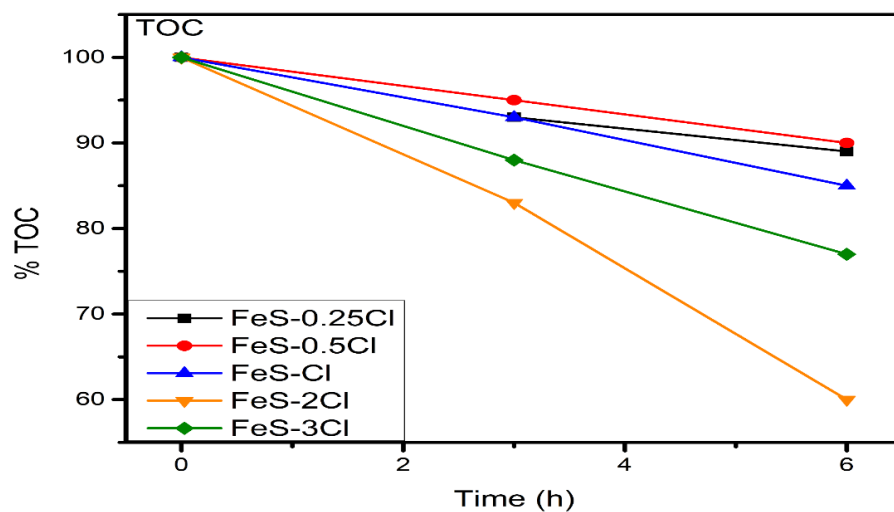


Figure 14. TOC results for FeS–0.25Cl, FeS–0.5Cl, FeS–2Cl and FeS–3Cl catalysts in visible-light region.

3. Discussion

Table 7 shows HYDRA-Medusa diagrams that presented the chemical equilibrium diagrams for the solution impregnation ratio iron/chlorine. In this sense, the catalysts Fe-0.25Cl, Fe-0.5Cl and Fe-1.0Cl presented 0.21, 0.41 and 0.70 FeCl fractions species, respectively. Additionally, the Fe-0.25Cl, Fe-0.5Cl and Fe-1.0Cl catalysts exhibited lower degradation. The Fe-2.0Cl and Fe-3.0Cl showed 0.85 FeCl fraction. Besides, the Fe-2.0Cl and Fe-3.0Cl catalysts displayed a higher photocatalytic activity than Fe-0.25Cl, Fe-0.5Cl and Fe-1.0Cl materials. At these ratios, 2.0 and 3.0, the area chemical equilibrium between FeCl species located in the interface region and OH groups of the titania support. K. Bourikas, C. Kordulis, and A. Lycourghiotis [45] extensively discussed the adsorption between supports and positive species complexes such as FeCl^+ , so it will be not considered in this paper.

Table 7. Chlorine fraction and degradation in the visible-light region.

Catalyst	Fe-Cl Fraction	Degradation
Fe-0.25Cl	0.21	12.53
Fe-0.5Cl	0.41	18.95
Fe-1.0Cl	0.70	16.64
Fe-2.0Cl	0.85	28.90
Fe-3.0Cl	0.85	26.70

DRS UV-Vis spectra showed a relation between the bandgap for oxide catalysts and the chlorine concentration presented on Figure 15. On the one hand, the bandgap of Fe-0.25Cl catalyst was 3.01 and the percentage degradation was about 29.0%. On the other hand, the addition of chlorine species increases the bandgap making suitable for visible-light activation. In this regard, the Fe-2Cl catalyst showed a bandgap value of 3.10 with higher degradation and mineralization percentage than Fe-0.25Cl. However, the excess concentrations of chlorine (Fe-3.0Cl) reduced the bandgap and decreased the degradation-mineralization ratio. According to above, the results suggested that chlorine addition increases the absorbance spectrum for visible-light activation increasing the photocatalytic activity. However, chlorine in the excess condition reduced the bandgap and mineralization.

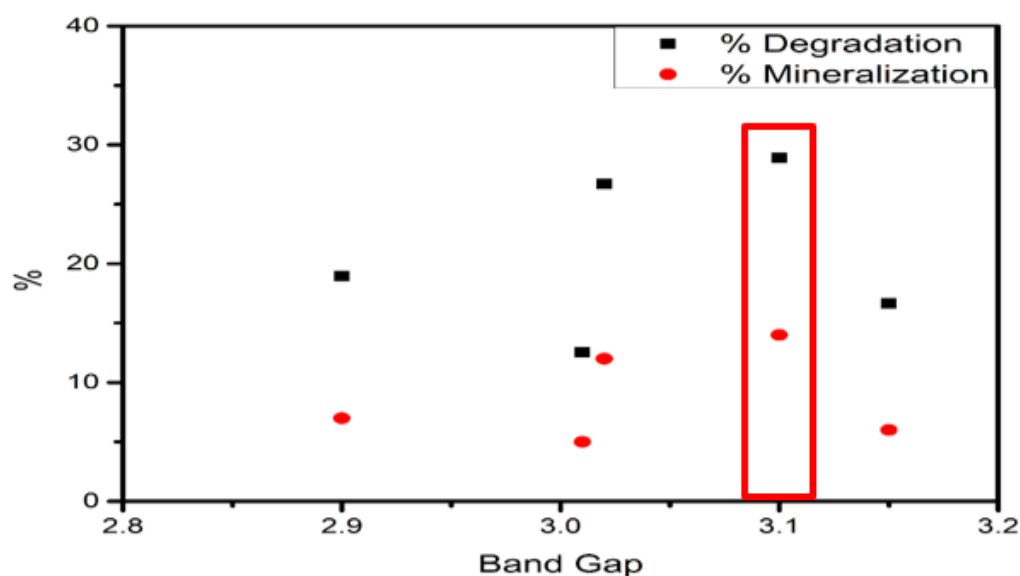


Figure 15. Oxide band gap vs. degradation and mineralization ratio.

Table 8 presents the $\text{Fe}^{2+}/\text{Fe}^{3+}$ ratio observed in TPR. The $\text{Fe}^{2+}/\text{Fe}^{3+}$ ratio showed that the degradation and mineralization incremented simultaneously until $\text{Fe}^{2+}/\text{Fe}^{3+}$ ratio at 0.77 (Figure 16). The $\text{Fe}^{2+}/\text{Fe}^{3+}$ at 0.84 exhibited a decrement of phenol degradation and mineralization. In this regard, the TPR results suggested that the addition of chlorine in the Fe photocatalyst increased the Fe^{2+} species and decreased redox temperature. In addition, the Fe^{2+} species promotes photoactivity and mineralization ratios.

Table 8. Catalyst temperatures and reduction areas.

Catalyst	Fe^{3+} Reduction	Area	Fe^{2+} Reduction	Area	$\text{Fe}^{2+}/\text{Fe}^{3+}$ Ratio
Fe-0.25Cl	423 °C	7099.04	705 °C	754.21	0.10
Fe-0.5Cl	482 °C	17,797.61	707 °C	1865.48	0.10
Fe-Cl	540 °C	16,684.97	711 °C	9459.16	0.56
Fe-2Cl	600 °C	4173.65	674 °C	3233.58	0.77
Fe-3Cl	590 °C	16,352.44	671 °C	13,804.88	0.84

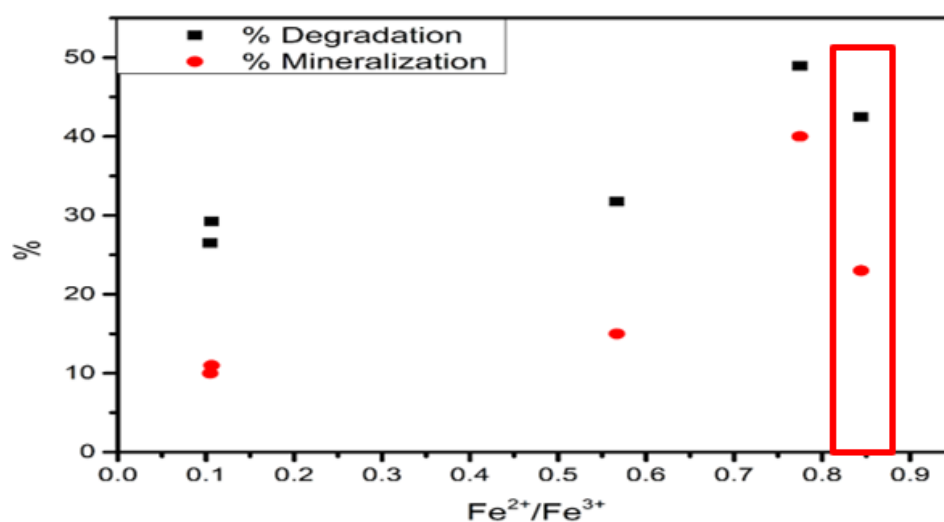


Figure 16. $\text{Fe}^{2+}/\text{Fe}^{3+}$ ratio vs. degradation and mineralization.

Figure 17 shows Fe^{2+} reduction temperature vs. degradation and mineralization activity. The Fe^{2+} reduction temperature at 670 °C presented 40% and 50% of phenol mineralization and degradation, respectively. The Fe^{2+} reduction temperature at 710 °C presented 10% and 20% of phenol mineralization and degradation, respectively. This result suggests that the temperature reduction in Fe^{2+} influenced on photocatalytic activity. The reduction in Fe^{2+} at a lower temperature is related to the moderate-strength metal–support interaction. The temperature shift in Fe^{2+} reduction could be related to an increment of sulfurization degree.

The diagrams HYDRA-MEDUSA and Raman results suggested that the formation of Fe-Cl species was replaced by sulphide species after the sulfurization process [46]. This behaviour could possibly be attributed to the formation of chlorine–sulphur bonds. In addition, chlorine–sulphur bonds are known to be unstable at ambient conditions [46]. The sulphide–oxide ratio is seen in Table 9 and Figure 18. The sulphide–oxide ratio results showed that the sulphurisation degree was similar for all catalysts.

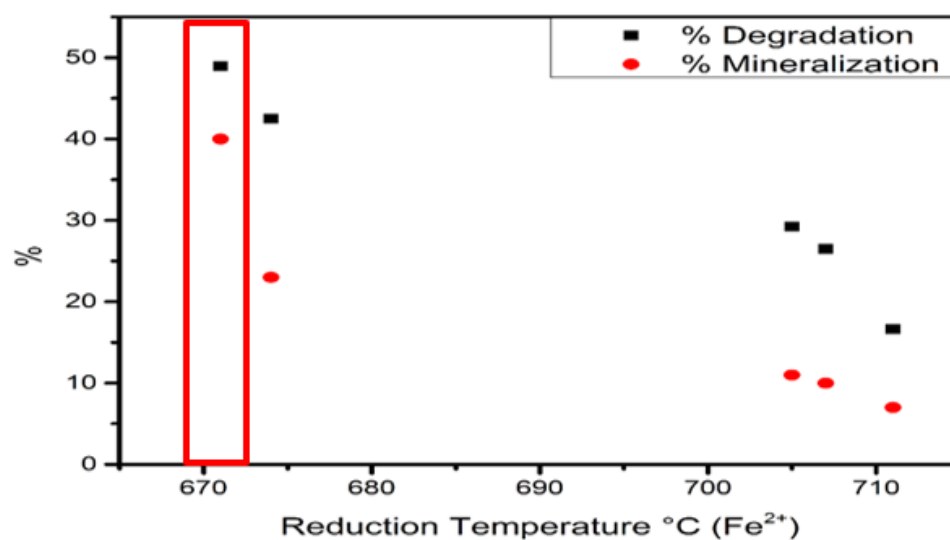


Figure 17. Fe^{2+} temperature reduction vs. degradation and mineralization percentage.

Table 9. Oxide–sulphide relation.

Catalyst	$\frac{\text{S}_y}{\text{O}_x}$ Raman	$\frac{\text{S}_y}{\text{O}_x}$ XPS	% Degradation	% Mineralization
FeS–0.25Cl	0.6243	0.6464	29.23	11
FeS–0.5Cl	0.6145	0.6404	26.49	10
FeS–Cl	0.6112	0.6351	31.73	15
FeS–2Cl	0.6095	0.6176	48.93	40
FeS–3Cl	0.6050	0.6038	42.49	23

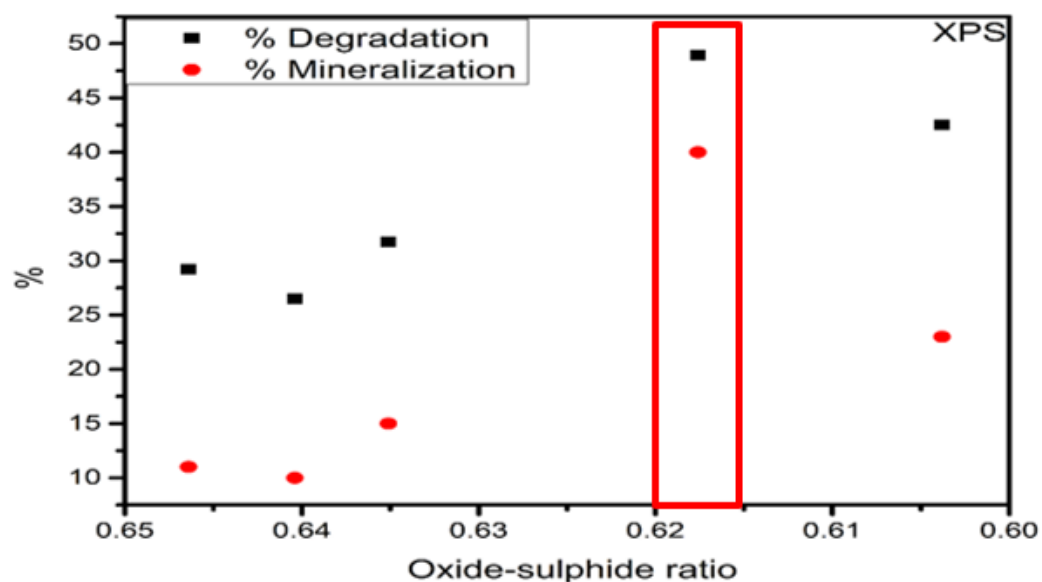
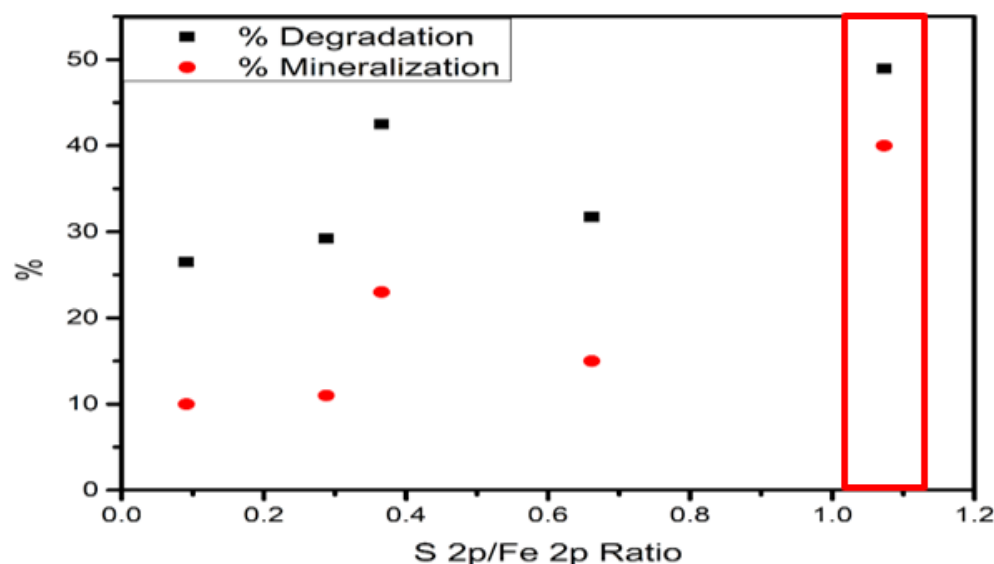


Figure 18. Sulphur–oxide versus degradation ratio.

In addition, the difference in photoactivity could be attributed to the formation of FeS species. In this sense, X-ray photoelectron spectra (XPS) at a low resolution were used to calculate the S and Fe ratios (Table 10 and Figure 19). The S/Fe ratio results indicated that species S promotes photoreactions and mineralization rates. Fe– S_y species presented higher activity than Fe– O_x species.

Table 10. S/Fe ratio.

XPS	FeS–0.25Cl	FeS–0.5Cl	FeS–Cl	FeS–2Cl	FeS–3Cl
S2p/Fe2p Ratio	0.2878	0.091	0.6617	1.073	0.3658

**Figure 19.** S2p/Fe2p vs. Degradation and Mineralization.

XPS diagrams were used to calculate bandgap after sulphurisation (Table 11 and Figure 20). The presence of S in the catalysts showed a 3% decrease in the bandgap. However, this slight decrease in bandgap was not attributed to photoactivity. An increase in activity can be attributed to the formation of FeS that provides reducing properties, promoting electron exchange. The bandgap of (3.05 eV) at equilibrium conditions (FeS–2Cl) achieved the highest degradation and mineralization rates.

Table 11. Oxide-band-gap to sulphide-band-gap ratio.

Catalyst	Band Gap O _x	Catalyst	Band Gap S _y	$\frac{Bg S_y}{Bg O_x}$	% Degradation	% Mineralization
Fe–0.25Cl	3.01	FeS–0.25Cl	2.90	0.96	29.23	11.0
Fe–0.5Cl	2.90	FeS–0.5Cl	2.82	0.97	26.49	10.0
Fe–Cl	3.15	FeS–Cl	3.10	0.98	31.73	15.0
Fe–2Cl	3.10	FeS–2Cl	3.05	0.98	48.93	40.0
Fe–3Cl	3.02	FeS–3Cl	2.95	0.97	42.49	23.0

The results suggested that the addition of chlorine on catalysts promotes the creation of Fe²⁺ species. In addition, Fe²⁺ species increase FeS formation rising phenol degradation and mineralization.

According to Dehua Xia, Yan Li, Guocheng Huang, Chi Ching Fong, Taicheng An, Guiying Li, Ho Yin Yip, Hunjun Zhao, Anhuai Lu, and Po Keung Wong, the conduction band (CB) of Fe₂O₃ is more favourable than that of FeS₂. Moreover, this has a more negative valence band (VB) than FeS₂. These suggestions led to the discovery that photogenerated electrons transfer from the CB of FeS₂ to the CB of Fe₂O₃ and, finally, to the VB of the FeS₂ [47]. The energy band configuration of the photocatalyst system could significantly promote the separation efficiency of photogenerated electron-hole pairs [42,48]. Additionally, some reports suggested that calcination at high temperatures and with a fast-heating rate could produce oxygen or sulphur vacancies in the mineral structure [49,50].

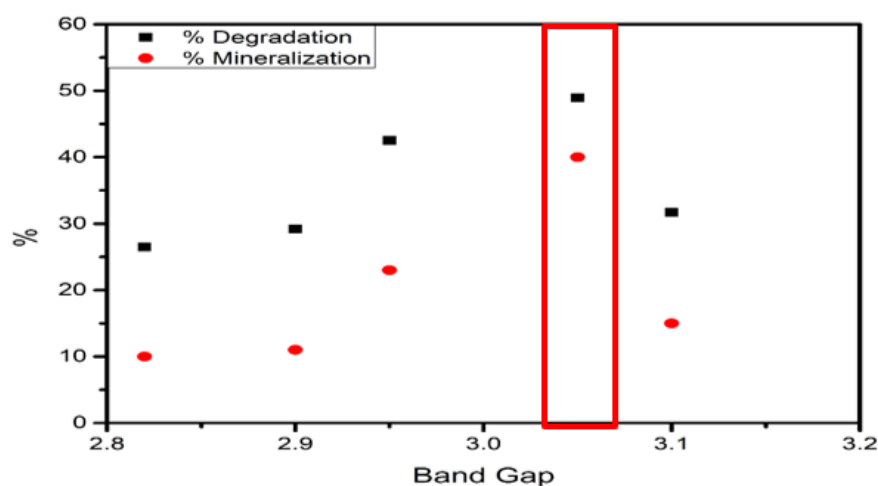


Figure 20. Sulphide band gap vs. degradation and mineralization ratio.

Figure 21 shows a proposed schematic diagram of the energy band configuration, obtained from conduction band and valence band values from XPS diagrams. Potential OH^* and O^* values were presented by Dehua Xia, Yan Li, Guocheng Huang, Chi Ching Fong, Taicheng An, Guiying Li, Ho Yin Yip, Hunjun Zhao, Anhuai Lu, and Po Keung Wong, 2015 [47]. Figure 21 shows the position of the valence and conduction band of FeS–Cl catalysts. The conduction band was obtained throughout XPS diagrams using the position of the Fermi level [44]. The valence band position was estimated by adding the band gap energy obtained from XPS O1s diagram. The E_g is the minimum energy required to excite an electron from the valence band to the conduction band. On the other hand, FeOx and FeSy phases are present in the sulfided materials. However, only one valence band and conduction band are shown for each one. In this regard, the FeSy–FeOx composite is a new material chemically linked with novelty physical and chemical properties. The band gap, the valence band and the conduction band can be tuned by modifying S/Fe composition. The reduction potential of the photogenerated electrons for the most active composite FeS–2Cl is more negative. Therefore, there was a larger energy available to perform the O_2/O_2^- production. The proposed results suggested that the potential formation of superoxide and peroxide ions produced a higher photocatalytic and mineralization ratio. Additionally, the possible formation of hydroxide and peroxide ions reduced the degradation–mineralization ratio.

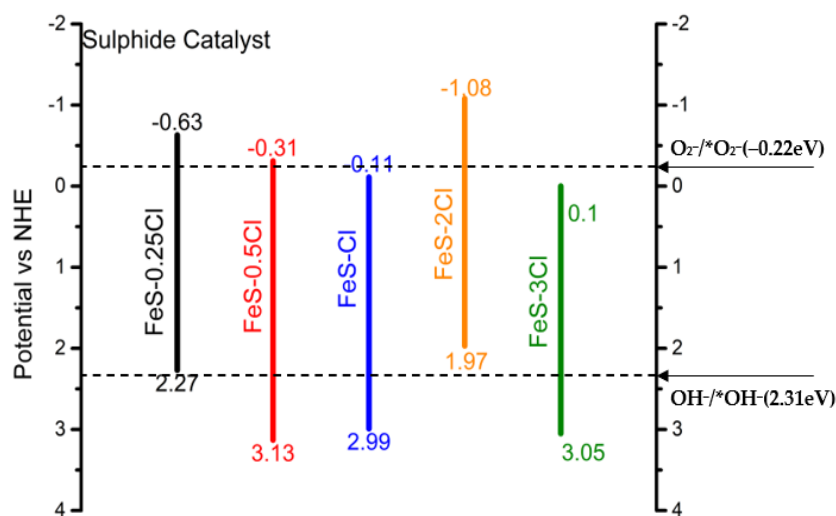


Figure 21. Proposed schematic diagram of the energy band configuration of sulphide catalyst heterojunction.

4. Materials and Methods

HYDRA program was used to calculate the fraction Fe and Cl species in solution. The iron and chlorine solutions were obtained from the salts FeN_3O_9 and NaCl, respectively. The iron solution at 5.68 M was modified with chlorine solution at different molar ratio Fe/Cl: 0.25, 0.5, 1.0, 2.0, 3.0. The synthesis of the catalysts was carried out by incipient impregnation. FeN_3O_9 salt was fixed at 0.82 gr corresponding to 10.0% w per 1.0 gr of catalyst. NaCl salt weight was modified according with the concentration desired. The ionized water volume was added in FeN_3O_9 and NaCl salts according to support total volume (0.35 mL per gram of support). This mixed solution was calcinated on a VULCAN 3-1750 furnace. Furnace conditions were:

- Ramp 1, drying: 5 °C per minute until reaching 120 °C and remained at that temperature for 3 h.
- Ramp 2, calcination: 10 °C per minute until reaching 300 °C and remained at that temperature for 5 h.
- Ramp 3, cooling: 5 °C per minute until reaching 50 °C and remained at that temperature for 3 h.

These catalysts were sulphated at 300 °C for 1 h and named by the acronyms: TiO_2S , FeS-0.25Cl/TiO_2 , FeS-0.5Cl/TiO_2 , FeS-Cl/TiO_2 , FeS-2Cl/TiO_2 , FeS-3Cl/TiO_2 .

Characterization of the Synthesized Photocatalysts

Raman spectrometry characterizations were performed with a Thermo Scientific DXR2 equipment with microscope. The sample was placed in the sampler of the equipment where it was analysed with the OMNIC program from 0 to 3500 Raman length, a general sweep was performed and a sweep to the bands of interest. Repetitions per catalyst were performed and an average of analysis was worked on for the appropriate study.

Diffuse reflectance technique (DRS UV-Vis) was obtained with a Cary-100 spectrophotometer using an optical length of 0.2 cm and a diffuse reflectance integrating sphere in the range of 190 to 400 nm, using barium sulphate (BaSO_4) as a reference.

Temperature-programmed reduction (TPR) experiments for solids were carried out on an AMI-90 apparatus (Altamira) equipped with a thermal conductivity detector (TCD). About 50 mg of a sample was placed in a quartz sample cell (U-shaped) for each analysis. The samples were pre-treated in situ at 373 K for 1 h under Air flow to remove fissured impurities. The reduction step was performed under a stream of (10 vol.%) H_2/Ar ($50 \text{ cm}^3 \text{ min}^{-1}$), with a heating rate of 10 K min^{-1} up to 1073 K. A thermal conductivity detector was used to determine variations in the hydrogen composition of the output stream. A moisture trap was used to avoid interferences in the measurements.

X-ray photoelectron spectrometry (XPS) equipment was used for the determination of oxidation states of components. Abundance and semi-quantitative analysis of components: Fe, S, Cl, Ti, O. Level binding energy: $2p_{3/2}$, $2p_{1/2}$ of Fe; $2p_{3/2}$, $2p_{1/2}$ of S; $2p_{3/2}$, $2p_{1/2}$ of Cl; $2p_{3/2}$, $2p_{1/2}$ of Ti; 1s of O. High resolution determination of Fe 2p in the region 730 to 700 eV; S 2p in the region 170 to 150 eV; Cl 2p in the region 204 to 194 eV; Ti 2p in the region 470 to 450 eV; O 1s in the region 540 to 520 eV. High resolution determination of C1s as a reference.

The photocatalytic visible-light reactions were carried out in a 0.75 L double jacketed Pyrex[®] batch reactor with a white LED lamp ($\lambda = 450 \text{ nm}$ and 550 nm , 78.5 W m^{-2}). The lamp was placed vertically at the top of the reactor, and airflow was added throughout the reaction. The phenolic solution was kept for 30 min under stirring (600 rpm) and in the dark for adequate dissolution of the contaminant. Subsequently, the catalyst was injected and kept for another 30 min under the same conditions to establish the adsorption pre-equilibrium; then, the lamp was switched on for six h. The samples were analysed in a UV-Vis Lambda 20 spectrometer and a Shimadzu TOC-Lcph/n total organic carbon (TOC) instrument for degradation, and mineralization rates, respectively. The amounts of catalyst and phenol were 1 g L^{-1} and 40 mg L^{-1} , respectively.

5. Conclusions

In summary, a novel material was developed for the photocatalytic degradation of phenol on visible-light irradiation. Sulphur addition increased photoactivity over 40% compared to oxide catalysts. The results indicated that adding chlorine to photocatalysts promotes the reduction state Fe^{3+} to Fe^{2+} , thus improving the formation of FeS species after sulphurisation having greater photocatalytic activity. However, excess chlorine conditions reduce sulphur species, reducing degradation and mineralization. For visible-light studies, sulphide species (Fe–S_y) maintain the bandgap and promote the formation of superoxide and peroxide ions, producing higher degradation and mineralization rates. In addition, oxide species (Fe–O_x) promote hydroxide and peroxide ions, producing high degradations levels but lower mineralization rates.

Author Contributions: D.A.-B.: Validation, Writing—original draft, Methodology, Investigation, Data curation, Formal analysis, Conceptualization. F.S.-M.: Resources, Supervision, Conceptualization, Project administration. V.S.: Supervision, Project administration, Conceptualization. I.C.R.-I.: Supervision, Visualization, Data curation, Project administration. J.A.d.l.R.H.: Resources, Funding acquisition, Visualization. R.R.-E.: Data curation, Project administration, Resources. F.T.-M.: Resources, Project administration, Visualization. C.E.S.-V.: Resources, Funding acquisition, Supervision, Writing—review & editing, Conceptualization. All authors have read and agreed to the published version of the manuscript.

Funding: This research was funded by Conacyt project “Desarrollo de innovaciones tecnológicas para una agricultura mexicana libre de Agroinsumos tóxicos” #316022, Project SIP-IPN #20221110 and #20220568.

Conflicts of Interest: The authors declare no conflict of interest.

References

1. Humayun, M.; Raziq, F.; Khan, A.; Luo, W. Modification strategies of TiO_2 for potential applications in photocatalysis: A critical review. *Green Chem. Lett. Rev.* **2018**, *11*, 86–102. [CrossRef]
2. Stagi, L.; Carbonaro, C.M.; Corpino, R.; Chiriu, D.; Ricci, P.C. Light induced TiO_2 phase transformation: Correlation with luminescent surface defects. *Phys. Status Solidi (B)* **2015**, *252*, 124–129. [CrossRef]
3. Moose. Summary of Environmental Law in Mexico. Available online: <https://moose.cec.org/moose/lawdatabase/mxdoc.cfm?varlan=english&topic=9> (accessed on 3 June 2003).
4. Anku, W.W.; Mamo, M.A.; Govender, P.P. Phenolic Compounds in Water: Sources, Reactivity, Toxicity and Treatment Methods. In *Phenolic Compounds—Natural Sources, Importance and Applications*; IntechOpen: London, UK, 2017; Available online: <https://www.intechopen.com/chapters/53973> (accessed on 10 April 2022).
5. Ghime, D.; Ghosh, P. Advanced Oxidation Processes: A Powerful Treatment Option for the Removal of Recalcitrant Organic Compounds. In *Advanced Oxidation Processes—Applications, Trends, and Prospects*; IntechOpen: London, UK, 2020; pp. 1–12.
6. Esplugas, S.; Giménez, J.; Contreras, S.; Pascual, E.; Rodríguez, M. Comparison of different advanced oxidation processes for phenol degradation. *Water Res.* **2002**, *36*, 1034–1042. [CrossRef]
7. Herrmann, J.M.; Duchamp, C.; Karkmaz, M.; Hoai, B.T.; Lachheb, H.; Puzenat, E.; Guillard, C. Environmental green chemistry as defined by photocatalysis. *J. Hazard. Mater.* **2007**, *146*, 624–629. [CrossRef] [PubMed]
8. Hoffmann, M.R.; Martin, S.T.; Choi, W.; Bahnemann, D.W. Environmental Applications of Semiconductor Photocatalysis. *Chem. Rev.* **1995**, *95*, 69–96. [CrossRef]
9. Maeda, K. Photocatalytic water splitting using semiconductor particles: History and recent developments. *J. Photochem. Photobiol. C Photochem. Rev.* **2011**, *12*, 237–268. [CrossRef]
10. Dursun, G.; Çiçek, H.; Dursun, A.Y. Adsorption of phenol from aqueous solution by using carbonised beet pulp. *J. Hazard. Mater.* **2005**, *125*, 175–182. [CrossRef]
11. Ugurlu, M.; Gurses, A.; Yalcin, M.; Dogar, C. Removal of phenolic and lignin compounds from bleached kraft mill effluent by fly ash and sepiolite. *Adsorption* **2005**, *11*, 87–97. [CrossRef]
12. Al-Kandari, H.; Abdullah, A.; Mohamed, A.; Al-Kandari, S. Enhanced photocatalytic degradation of a phenolic compounds' mixture using a highly efficient TiO_2 /reduced graphene oxide nanocomposite. *J. Mater. Sci.* **2016**, *51*, 8331–8345. [CrossRef]
13. Zhu, Y.; Liu, Y.; Ai, Q.; Gao, G.; Yuan, L.; Fang, Q.; Tian, X.; Zhang, X.; Egap, E.; Ajayan, P.M.; et al. In Situ Synthesis of Lead-Free Halide Perovskite-COF Nanocomposites as Photocatalysts for Photoinduced Polymerization in Both Organic and Aqueous Phases. *ACS Mater. Lett.* **2022**, *4*, 464–471. [CrossRef]
14. Abdollahi, Y.; Abdullah, A.H.; Zainal, Z.; Yusof, N.A. Photocatalytic degradation of *p*-Cresol by zinc oxide under UV irradiation. *Int. J. Mol. Sci.* **2012**, *13*, 302–315. [CrossRef] [PubMed]

15. Zhang, J.; Ma, J.; Zhang, S.; Wang, W.; Chen, Z. A highly sensitive nonenzymatic glucose sensor based on CuO nanoparticles decorated carbon spheres. *Sens. Actuators B Chem.* **2015**, *211*, 385–391. [CrossRef]
16. Feng, Y.-B.; Hong, L.; Liu, A.-L.; Chen, W.-D.; Li, G.-W.; Chen, W.; Xia, X.-H. High-efficiency catalytic degradation of phenol based on the peroxidase-like activity of cupric oxide nanoparticles. *Int. J. Environ. Sci. Technol.* **2015**, *12*, 653–660. [CrossRef]
17. Mirian, Z.-A.; Nezamzadeh-Ejehieh, A. Removal of phenol content of an industrial wastewater via a heterogeneous photodegradation process using supported FeO onto nanoparticles of Iranian clinoptilolite. *Desalination Water Treat.* **2016**, *57*, 16483–16494. [CrossRef]
18. Shahrezaei, F.; Akhbari, A.; Rostami, A. Photodegradation and removal of phenol and phenolic derivatives from petroleum refinery wastewater using nanoparticles of TiO₂. *Int. J. Energy Environ.* **2012**, *3*, 267–274.
19. Zeng, G.; Zhang, Q.; Liu, Y.; Zhang, S.; Guo, J. Preparation of TiO₂ and Fe-TiO₂ with an Impinging Stream-Rotating Packed Bed by the Precipitation Method for the Photodegradation of Gaseous Toluene. *Nanomaterials* **2019**, *9*, 1173. [CrossRef]
20. Cao, Z.; Zhang, T.; Ren, P.; Cao, D.; Lin, Y.; Wang, L.; Zhang, B.; Xiang, X. Doping of Chlorine from a Neoprene Adhesive Enhances Degradation Efficiency of Dyes by Structured TiO₂-Coated Photocatalytic Fabrics. *Catalysts* **2020**, *10*, 69. [CrossRef]
21. Niu, Y.; Xing, M.; Zhang, J.; Tian, B. Visible light activated sulfur and iron co-doped TiO₂ photocatalyst for the photocatalytic degradation of phenol. *Catal. Today* **2013**, *201*, 159–166. [CrossRef]
22. Royal Institute of Technology. Kungliga Tekniska högskolan Chemical Equilibrium Diagrams 2016. Available online: <https://www.kth.se/che/medusa/downloads-1.386254> (accessed on 10 April 2022).
23. Oelkers, E.H.; Helgeson, H.C. Triple-ion anions and polynuclear complexing in supercritical electrolyte solutions. *Geochim. Cosmochim. Acta* **1990**, *54*, 727–738. [CrossRef]
24. Suárez-Toriello, V.A.; Santolalla-Vargas, C.E.; de los Reyes, J.A.; Vázquez-Zavala, A.; Vrinat, M.; Geantet, C. Influence of the solution pH in impregnation with citric acid and activity of Ni/W/Al₂O₃ catalysts. *J. Mol. Catal. A Chem.* **2015**, *404–405*, 36–46. [CrossRef]
25. Bielan, Z.; Dudziak, S.; Sulowska, A.; Pelczarski, D.; Ryl, J.; Zielińska-Jurek, A. Preparation and Characterization of Defective TiO₂. The Effect of the Reaction Environment on Titanium Vacancies Formation. *Materials* **2020**, *13*, 2763. [CrossRef] [PubMed]
26. Lerici, L.; Femanelli, C.; Diguilio, E.; Pierella, L.; Saux, C. Síntesis y caracterización de fotocatalizadores de hierro soportado sobre zeolitas microporosas. *Matéria* **2018**, *23*, 450. [CrossRef]
27. Samanta, S.; Giri, S.; Sastry, P.U.; Mal, N.K.; Manna, A.; Bhaumik, A. Synthesis and Characterization of Iron-Rich Highly Ordered Mesoporous Fe-MCM-41. *Ind. Eng. Chem. Res.* **2003**, *42*, 3012–3018. [CrossRef]
28. Wang, J.-C.; Ren, J.; Yao, H.C.; Zhang, L.; Wang, J.S.; Zang, S.Q.; Li, Z.J. Synergistic photocatalysis of Cr(VI) reduction and 4-Chlorophenol degradation over hydroxylated α -Fe₂O₃ under visible light irradiation. *J. Hazard. Mater.* **2016**, *311*, 11–19. [CrossRef] [PubMed]
29. Abbott, A.P.; Al-Bassam, A.Z.; Goddard, A.; Harris, R.C.; Jenkin, G.R.; Nisbet, F.J.; Wieland, M. Dissolution of pyrite and other Fe–S–As minerals using deep eutectic solvents. *Green Chem.* **2017**, *19*, 2225–2233. [CrossRef]
30. Makuła, P.; Pacia, M.; Macyk, W. How To Correctly Determine the Band Gap Energy of Modified Semiconductor Photocatalysts Based on UV–Vis Spectra. *J. Phys. Chem. Lett.* **2018**, *9*, 6814–6817. [CrossRef] [PubMed]
31. Lv, H.; Zhao, H.; Cao, T.; Qian, L.; Wang, Y.; Zhao, G. Efficient degradation of high concentration azo-dye wastewater by heterogeneous Fenton process with iron-based metal-organic framework. *J. Mol. Catal. A Chem.* **2015**, *400*, 81–89. [CrossRef]
32. Fakeeha, A.H.; Ibrahim, A.A.; Naeem, M.A.; Khan, W.U.; Abasaheed, A.E.; Alotaibi, R.L.; Al-Fatesh, A.S. Methane decomposition over Fe supported catalysts for hydrogen and nano carbon yield. *Catal. Sustain. Energy* **2015**, *2*, 71–82. [CrossRef]
33. El-Deen, S.S.; Hashem, A.M.; Abdel Ghany, A.E.; Indris, S.; Ehrenberg, H.; Mauger, A.; Julien, C.M. Anatase TiO₂ nanoparticles for lithium-ion batteries. *Ionics* **2018**, *24*, 2925–2934. [CrossRef]
34. Song, C.; Wang, S.; Dong, W.; Fang, X.; Shao, J.; Zhu, J.; Pan, X. Hydrothermal synthesis of iron pyrite (FeS₂) as efficient counter electrodes for dye-sensitized solar cells. *Sol. Energy* **2016**, *133*, 429–436. [CrossRef]
35. Li, Y.-S.; Church, J.S.; Woodhead, A.L. Infrared and Raman spectroscopic studies on iron oxide magnetic nano-particles and their surface modifications. *J. Magn. Magn. Mater.* **2012**, *324*, 1543–1550. [CrossRef]
36. Wang, X.; Xiang, Q.; Liu, B.; Wang, L.; Luo, T.; Chen, D.; Shen, G. TiO₂ modified FeS Nanostructures with Enhanced Electrochemical Performance for Lithium-Ion Batteries. *Sci. Rep.* **2013**, *3*, 2007. [CrossRef] [PubMed]
37. Yan, Z.; Zhuxia, Z.; Tianbao, L.; Xuguang, L.; Bingshe, X. XPS and XRD study of FeCl₃-graphite intercalation compounds prepared by arc discharge in aqueous solution. *Spectrochim. Acta Part A Mol. Biomol. Spectrosc.* **2008**, *70*, 1060–1064. [CrossRef] [PubMed]
38. Usha, N.; Viswanathan, B.; Murthy, V.R.K.; Sobhanadri, J. X-ray photoelectron spectroscopic study of some pure stages of graphite ferric chloride intercalation compounds. *Spectrochim. Acta Part A Mol. Biomol. Spectrosc.* **1997**, *53*, 1761–1765. [CrossRef]
39. Luo, Y.; Luo, J.; Jiang, J.; Zhou, W.; Yang, H.; Qi, X.; Zhang, H.; Fan, H.J.; Yu, D.Y.W.; Li, C.M.; et al. Seed-assisted synthesis of highly ordered TiO₂@ α -Fe₂O₃ core/shell arrays on carbon textiles for lithium-ion battery applications. *Energy Environ. Sci.* **2012**, *5*, 6559–6566. [CrossRef]
40. Ramírez-Salgado, J.; Quintana-Solórzano, R.; Mejía-Centeno, I.; Armendáriz-Herrera, H.; Rodríguez-Hernández, A.; Guzmán-Castillo, M.d.L.; Valente, J.S. On the role of oxidation states in the electronic structure via the formation of oxygen vacancies of a doped MoVTeNbOx in propylene oxidation. *Appl. Surf. Sci.* **2022**, *573*, 151428. [CrossRef]

41. Miyazaki, S.; Nishimura, H.; Fukuda, M.; Ley, L.; Ristein, J. Structure and electronic states of ultrathin SiO₂ thermally grown on Si(100) and Si(111) surfaces. *Appl. Surf. Sci.* **1997**, *113–114*, 585–589. [[CrossRef](#)]
42. Scanlon, D.O.; Dunnill, C.W.; Buckeridge, J.; Shevlin, S.A.; Logsdail, A.J.; Woodley, S.M.; Catlow, C.R.A.; Powell, M.J.; Palgrave, R.G.; Parkin, I.P.; et al. Band alignment of rutile and anatase TiO₂. *Nat. Mater.* **2013**, *12*, 798–801. [[CrossRef](#)]
43. Grant, R.W.; Kraut, E.A.; Kowalczyk, S.P.; Waldrop, J.R. Measurement of potential at semiconductor interfaces by electron spectroscopy. *J. Vac. Sci. Technol. B Microelectron. Process. Phenom.* **1983**, *1*, 320–327. [[CrossRef](#)]
44. Kraut, E.A.; Grant, R.W.; Waldrop, J.R.; Kowalczyk, S.P. Precise Determination of the Valence-Band Edge in X-ray Photoemission Spectra: Application to Measurement of Semiconductor Interface Potentials. *Phys. Rev. Lett.* **1980**, *44*, 1620–1623. [[CrossRef](#)]
45. Bourikas, K.; Kordulis, C.; Lycourghiotis, A. The Role of the Liquid-Solid Interface in the Preparation of Supported Catalysts. *Catal. Rev.* **2006**, *48*, 363–444. [[CrossRef](#)]
46. Lindquist, B.A.; Dunning, T.H. The nature of the SO bond of chlorinated sulfur–oxygen compounds. *Theor. Chem. Acc.* **2014**, *133*, 1443. [[CrossRef](#)]
47. Xia, D.; Li, Y.; Huang, G.; Fong, C.C.; An, T.; Li, G.; Yip, H.Y.; Zhao, H.; Lu, A.; Wong, P.K. Visible-light-driven inactivation of *Escherichia coli* K-12 over thermal treated natural pyrrhotite. *Appl. Catal. B Environ.* **2015**, *176–177*, 749–756. [[CrossRef](#)]
48. Zhou, P.; Yu, J.; Jaroniec, M. All-Solid-State Z-Scheme Photocatalytic Systems. *Adv. Mater.* **2014**, *26*, 4920–4935. [[CrossRef](#)]
49. Warschkow, O.; Ellis, D.; Hwang, J.; Mansourian-Hadavi, N.; Mason, T. Defects and Charge Transport near the Hematite (0001) Surface: An Atomistic Study of Oxygen Vacancies. *J. Am. Ceram. Soc.* **2002**, *85*, 213–220. [[CrossRef](#)]
50. Birkholz, M.; Fiechter, S.; Hartmann, A.; Tributsch, H. Sulfur deficiency in iron pyrite FeS_{2-x} and its consequences for band-structure models. *Phys. Rev. B* **1991**, *43*, 11926–11936. [[CrossRef](#)]